EQUILIBRIUM PATHS OF MECHANICAL SYSTEMS WITH UNILATERAL CONSTRAINTS PART II: DEPLOYABLE REFLECTOR

M. Schulz * and S. Pellegrino†

Abstract

The paper presents a simulation of the deployment/retraction of a solid surface deployable reflector recently developed at Cambridge University. The simulation takes proper account of the contacts that can develop between panels of adjacent wings of the reflector, by implementing the theory for tracing the equilibrium path of a mechanical system with unilateral constraints that has been proposed in the companion paper. Six-fold symmetry is assumed, as experiments on a physical model of the reflector show that asymmetries do not play a significant role. During deployment, at a certain point the model shows a sudden increase in the rate of motion although the (slow) rate of turning of the electric motors driving the model remains uniform. It is shown that the reason for this behaviour, which had not been previously explained, is the existence of a corner limit point on the equilibrium path of this structure. A corner limit point is a kind of limit point that can be encountered only in systems with unilateral constraints; the equilibrium path is non-smooth and the first-order equilibrium equations non-singular. A second limit point, of the standard type, exists on the equilibrium path. It should cause the model to jump to a configuration close to fully folded, but cannot be achieved in practice. A characteristic conical shape of the physical model is observed at the end of the retraction and is predicted by the simulation as well.

(Key words: Solid Surface Deployable Antenna, Multibody Systems, Unilateral Constraint, Limit Point, Snap-through)

*Dept. FV/SLT2 Robert Bosch GmbH, P.O. Box 30 02 40, 70442 Stuttgart, Germany. Marcus.Schulz2@de.bosch.com

†Corresponding author. Department of Engineering, University of Cambridge, Trumpington Street, Cambridge, CB2 1PZ, UK. pellegrino@eng.cam.ac.uk

1 Introduction

In the companion paper (Schulz and Pellegrino 1999) we have presented a general theory for tracing the equilibrium path of multibody systems that are subject to unilateral constraints. The development of that theory was motivated by the need to properly simulate the behaviour of a solid surface deployable reflector recently developed in the Deployable Structures Laboratory at the University of Cambridge (Guest and Pellegrino 1996). The key aim of the present paper is to apply our theory to this particular deployable reflector, and thus explain some anomalies that were observed during experiments conducted on a physical model of the reflector.

The concept of the reflector is shown in Figure 1. Figure 1(a) shows a front view of the antenna surface, split into six wings; each wing is further subdivided into five panels, connected by revolute joints; adjacent wings are linked by connecting rods, also through revolute joints. Figure 1(b) shows how these wings and panels fit together after folding; the panels are shown flat for clarity, but the same kind of nested arrangement is also possible for curved panels. The reflector is deployed by synchronously driving, by means of electric motors, the six joints between the connecting rods and the last panel of each wing. This produces a complex, symmetric three-dimensional motion of the structure, shown in Figure 2, in which the wings first unwrap and then rotate about the hub. Ideally, this motion should not require any deformation of the structure, but due to the complexity of its geometry and to the constraints imposed by hinge stops and panel contacts, it is impossible to find a layout of the hinges such that this structure is a perfect mechanism for the complete range of motion involved in the deployment process. A practical solution is to accept a small amount of elastic deformation, and this is the strategy that was adopted in the case of the reflector.

A physical model of this reflector, whose geometric layout had been designed by minimising the peak strain energy during deployment, was manufactured and tested by Guest and Pellegrino (1996). The model worked fine during deployment, but was unable to retract automatically. It had been expected that its behaviour during retraction would mirror the deployment behaviour but, when the direction of turning of the motorised hinges was reversed, the model started to follow an incorrect path. It could either be allowed to continue along this path until the motors had to be stopped to avoid damaging the model, or the configuration of the model could be manually rectified, after which automatic retraction to the correct packaged configuration could be successfully completed.

Detailed measurements of the configuration of the model during deployment (Gardiner 1995)

showed its motion to be less regular and symmetric than it might be expected from the regularity and symmetry of the motion imparted by the motors. Initial attempts at simulating the continuous deployment motion of the reflector, as opposed to the computation of separate states of least energy performed during the design of the model, run into difficulties. It was discovered that if the unilateral constraints acting between different parts of the reflector are not modelled properly, it appears to be able to follow many different equilibrium paths. In the absence of a proper theoretical formulation for simulating the motion of this kind of multibody system, it wasn't possible to go any further at that stage.

Schulz and Pellegrino (1998) have recently shown that the kind of "multi-path" behaviour observed in this model reflector can occur in general multibody systems consisting of rigid links and elastic springs. For this behaviour to occur, the equilibrium path of the system must exhibit two (or more) limit points, so that during deployment the system loses stability when it reaches the first limit point, and snaps to a stable part of the path. During retraction the system loses stability and snaps, at a different limit point. If the retraction path is stable until the control parameter of the system, e.g. in the model reflector the rotation angle of the motorised hinges, reaches its final value the system ends up in a retracted configuration that is actually different from that at the start of the deployment cycle.

A detailed analysis of several mechanical systems that are subject to bilateral constraints only has shown that the behaviour described above occurs, for a given system, only for a small range of values of its elastic parameters. The situation is considerably different in systems with unilateral constraints. In the companion paper we have shown that a new kind of limit point, called *corner limit point*, can exist in such systems. Unlike common limit points, which require the reduced Hessian matrix of the system to be singular, a corner limit point requires only a non-positive definite reduced Hessian. Because there are two types of limit points, in systems with unilateral constraints there is a greater variety of limiting behaviour compared to systems with bilateral constraints only. Thus, it appears to be much easier for a system with unilateral constraints to exhibit multi-path behaviour than it would be for a "similar" system with bilateral constraints only.

The paper is laid out as follows. Section 2 introduces a simple model of the reflector, whose elastic deformation is assumed to be concentrated in the link between the connecting rod of wing i and wing $i+1$. Section 3 determines analytical expressions for the derivatives of the potential energy of the system that are required for the computations described in the companion paper.

Section 4 presents an analytical formulation for the unilateral constraints present in the system, which include hinge stops and possible contacts between panels of adjacent wings. Section 5 presents a simulation of the quasi-static deployment and retraction of the system. Having traced the complete equilibrium path of the system, we identify and plot the sequence of stable configurations that we would expect to see in the physical model. These configurations are compared to photographs of the model in different configurations, and to measurements taken from it, in Section 6. It is found that almost all features of the behaviour predicted are observed in practice. There is only one significant difference, which can be easily explained. A Discussion concludes the paper.

2 Modelling the physical system

The reflector is modelled as an assembly of flat, rigid panels of zero thickness, with the regular geometry shown in Figure 3. This will considerably simplify the formulation of the contact problems without any significant loss of accuracy. Also, the edge of panel 5 will be assumed to be straight, instead of curved, for simplicity. The overall topology of the structure, however, is not simplified.

Deployment and retraction of the reflector are assumed to be six-fold symmetric, hence the configuration of the complete reflector is fully defined by the configuration of wing 1. Therefore, modelling the connection between two consecutive panels as a rigid, frictionless revolute joint, the configuration of wing 1 is completely described by the five rotations of these joints, plus the angle between panel 5 and the connecting rod.

Right-handed coordinate sets are defined for the hub and each panel of wing 1, as shown in Figure 4. The coordinate sets (x, y, z), at the centre of the hub, and (x_1, y_1, z_1) are both attached to the hub; (x_2, y_2, z_2) is attached to panel 1, etc. The coordinate set (x_7, y_7, z_7) is attached to the connecting rod. The definition of these coordinate sets is such that we are able to describe the kinematics of the system by using the well-known Denavit-Hartenberg notation (Denavit and Hartenberg 1955).

Note that all z_i-axes are aligned with a revolute joint, apart from z and z_7. Our six configuration parameters are the angles between x_i and x_{i+1} (about z_i), φ_i with $i = \{1, \ldots, 5\}$, plus the angle, p, between x_7 and x_6 (about z_6). Angle φ_1 defines the relative rotation between panel 1 and the hub, φ_2 between panel 2 and panel 1, etc., and p the relative rotation between

the connecting rod and panel 5.

In the fully deployed configuration these parameters have the values $\varphi_1 = -90°$, $\varphi_2 = 90°$, $\varphi_3 = 0$, $\varphi_4 = 0$, $\varphi_5 = -90°$ and $p = 0$. In the fully-folded configuration they have the values $\varphi_1 = -180°$, $\varphi_2 = 30°$, $\varphi_3 = -60°$, $\varphi_4 = -60°$, $\varphi_5 = -150°$ and $p = -180°$.

In the physical model the joint between the connecting rod and panel 4 of the following wing is realised by means of a hinge attached to an angle bracket, Figure 5, whose compliance in the direction of the bar is modelled by introducing two identical extensional springs. In the simulation model these springs are attached to points S1 and S3 of the connecting rod and to points S2 and S4 of panel 4 on wing 2, respectively; these points are defined in Figure 3. These springs are unstrained in the fully-deployed and fully-folded configurations, because everything fits together in these two configurations, hence the global coordinates of points S1 and S2, and also of S3 and S4, are equal in these two configurations. During deployment/retraction these springs have to deform because, as discussed in Section 1, the structure is not a perfect mechanism. However, because all other parts of the physical model are much stiffer than the connecting rod brackets, the model is assumed to be rigid apart from these springs.

Denoting by s_i the coordinates of the spring attachment point, S_i, in the hub-centred coordinate system x, y, z

$$s_i = \left[\begin{array}{ccc} x(Si) & y(Si) & z(Si) \end{array} \right]^T, \quad i = 1, \ldots, 4 \quad . \tag{1}$$

Assuming the springs to have zero unstrained length and stiffness k, the potential energy U of the reflector in a general configuration is

$$U = 6\frac{k}{2}\left[(s_2 - s_1)^T (s_2 - s_1) + (s_4 - s_3)^T (s_4 - s_3) \right] \quad , \tag{2}$$

Note that Equation 2 neglects the potential energy of the reflector due to gravity, in the assumption that the reflector will be operated either in a gravity-free environment, or if there is gravity in conjuction with a perfect gravity compensation system.

3 Kinematic formulation

This section derives expressions for the second-order derivatives of U, from which $\nabla^2_\varphi U$ and $\nabla_\varphi U'$ —required for the computation of the equilibrium path, see Section 3 of the companion paper— can be obtained.

Applying the formalism proposed by Denavit and Hartenberg (1955) the position vectors s_i are represented by 4-vectors[1]

$$ {}^4s_i = \begin{bmatrix} 1 & s_i \end{bmatrix}^T, \quad i = 1, \ldots, 4 \tag{3} $$

Analytical expressions for these vectors are obtained by compounding the rigid-body rotations between the sets of axes introduced in Section 2. Thus, the following functions of the generalized coordinates φ_i and the control parameter p are obtained

$$ {}^4s_1 = A_1 B_1 B_2 B_3 B_4 B_5 P \; {}^4\xi_1 \quad , \tag{4} $$

$$ {}^4s_2 = A_2 B_1 B_2 B_3 B_4 \; {}^4\xi_2 \quad , \tag{5} $$

$$ {}^4s_3 = A_1 B_1 B_2 B_3 B_4 B_5 P \; {}^4\xi_3 \quad , \tag{6} $$

$$ {}^4s_4 = A_2 B_1 B_2 B_3 B_4 \; {}^4\xi_4 \quad . \tag{7} $$

Note that the above equations have the same basic structure. The A_i matrices represent the transformation from the hub-centred set of axes to the first set, (x_1, y_1, z_1); the matrix for wing 2, A_2, is obtained by rotating the matrix for wing 1, A_1, through 60°. The B_i matrices represent the transformation from one panel to the next. The P matrix represents the transformation from the connecting rod to panel 5. The 4-vectors ${}^4\xi_i$ are the coordinates of the spring attachment points with respect to the coordinate system for panel 4, points S_2 and S_4, and the connecting rod, points S_1 and S_3.

The matrices, A_i and the vectors ${}^4\xi_i$ do not vary with the configuration of the system, but depend only on the length L

$$ A_1 = \begin{bmatrix} 1 & 0 & 0 & 0 \\ 0 & 0 & 0 & 1 \\ -\sqrt{3}L/2 & -1 & 0 & 0 \\ 0 & 0 & -1 & 0 \end{bmatrix}, \quad A_2 = \begin{bmatrix} 1 & 0 & 0 & 0 \\ 3L/4 & \sqrt{3}/2 & 0 & 1/2 \\ -\sqrt{3}L/4 & -1/2 & 0 & \sqrt{3}/2 \\ 0 & 0 & -1 & 0 \end{bmatrix}, \tag{8} $$

$$ {}^4\xi_1 = \begin{bmatrix} 1 & 0 & 0 & -3L \end{bmatrix}^T, \quad {}^4\xi_2 = \begin{bmatrix} 1 & -L & 0 & 0 \end{bmatrix}^T, $$

$$ {}^4\xi_3 = \begin{bmatrix} 1 & 0 & 0 & -4L \end{bmatrix}^T, \quad {}^4\xi_4 = \begin{bmatrix} 1 & 0 & 0 & 0 \end{bmatrix}^T. \tag{9} $$

[1]The four components of these vectors are the *homogeneous coordinates* of a point; for a point not at infinity one of the four coordinates is usually taken as 1.

Each matrix B_i is a function of one coordinate φ_i

$$
\begin{aligned}
B_1 &= \begin{bmatrix} 1 & 0 & 0 & 0 \\ 0 & \cos\varphi_1 & 0 & \sin\varphi_1 \\ 0 & \sin\varphi_1 & 0 & -\cos\varphi_1 \\ L/2 & 0 & 1 & 0 \end{bmatrix}, \\
B_i &= \begin{bmatrix} 1 & 0 & 0 & 0 \\ L\cos\varphi_i & \cos\varphi_i & -\sin\varphi_i & 0 \\ L\sin\varphi_i & \sin\varphi_i & \cos\varphi_i & 0 \\ 0 & 0 & 0 & 1 \end{bmatrix}, \quad i = 2,3,4 \quad , \\
B_5 &= \begin{bmatrix} 1 & 0 & 0 & 0 \\ 0 & \cos\varphi_5 & (\sin\varphi_5)/2 & (\sqrt{3}\sin\varphi_5)/2 \\ 0 & \sin\varphi_5 & -(\cos\varphi_5)/2 & (-\sqrt{3}\cos\varphi_5)/2 \\ \sqrt{3}L & 0 & \sqrt{3}/2 & -1/2 \end{bmatrix}.
\end{aligned}
\tag{10}
$$

and the matrix P depends only on the control parameter p

$$
P = \begin{bmatrix} 1 & 0 & 0 & 0 \\ 0 & \cos p & (-\sqrt{3}\sin p)/2 & (\sin p)/2 \\ 0 & \sin p & (\sqrt{3}\cos p)/2 & -(\cos p)/2 \\ 2\sqrt{3}L & 0 & 1/2 & \sqrt{3}/2 \end{bmatrix} \quad . \tag{11}
$$

An important advantage of having adopted the Denavit-Hartenberg formalism is that the derivatives with respect to the generalized coordinate φ_i or the control parameter p can be easily computed by premultiplying B_i and P by the matrix

$$
D = \begin{bmatrix} 0 & 0 & 0 & 0 \\ 0 & 0 & -1 & 0 \\ 0 & 1 & 0 & 0 \\ 0 & 0 & 0 & 0 \end{bmatrix} \quad , \tag{12}
$$

see Denavit et al. (1965). Examples of first and second-order derivatives are

$$
\begin{aligned}
{}^4s_{1,\varphi_2} &= A_1B_1DB_2B_3B_4B_5P\ {}^4\xi_1 \quad , & {}^4s'_3 &= A_1B_1B_2B_3B_4B_5DP\ {}^4\xi_3 \quad , \\
{}^4s_{2,\varphi_2\varphi_4} &= A_2B_1DB_2B_3DB_4\ {}^4\xi_2 \quad , & {}^4s_{4,\varphi_3\varphi_3} &= A_2B_1B_2D^2B_3B_4\ {}^4\xi_4 \quad , \\
{}^4s'_{3,\varphi_2} &= A_1B_1DB_2B_3B_4B_5DP\ {}^4\xi_3 \quad , & {}^4s'_2 &= {}^4s_{2,\varphi_5} = {}^4s'_4 = {}^4s_{4,\varphi_5} = 0 \quad ,
\end{aligned}
$$

where $(\quad)'$ indicates partial differentiation with respect to the control parameter p, and partial differentiation with respect to a generalized coordinate is denoted by a subscript φ_i. Therefore, the derivatives of the potential energy are

$$\begin{aligned} U'_{,\varphi_i} &= 6k \Big[{}^4s_1'^T \left({}^4s_{1,\varphi_i} - {}^4 s_{2,\varphi_i} \right) + \left({}^4s_1 - {}^4 s_2 \right)^T {}^4s'_{1,\varphi_i} \\ &\quad + {}^4s_3'^T \left({}^4s_{3,\varphi_i} - {}^4 s_{4,\varphi_i} \right) + \left({}^4s_3 - {}^4 s_4 \right)^T {}^4s'_{3,\varphi_i} \Big] \ , \qquad (13) \\ U_{,\varphi_i\varphi_j} &= 6k \Big[\left({}^4s_{1,\varphi_j} - {}^4 s_{2,\varphi_j} \right)^T \left({}^4s_{1,\varphi_i} - {}^4 s_{2,\varphi_i} \right) + \left({}^4s_1 - {}^4 s_2 \right)^T \left({}^4s_{1,\varphi_i\varphi_j} - {}^4 s_{2,\varphi_i\varphi_j} \right) \\ &+ \left({}^4s_{3,\varphi_j} - {}^4 s_{4,\varphi_j} \right)^T \left({}^4s_{3,\varphi_i} - {}^4 s_{4,\varphi_i} \right) + \left({}^4s_3 - {}^4 s_4 \right)^T \left({}^4s_{3,\varphi_i\varphi_j} - {}^4 s_{4,\varphi_i\varphi_j} \right) \Big] \ . \qquad (14) \end{aligned}$$

4 Formulation of constraints

Potential contacts between parts of the reflector can, theoretically, develop in many different ways but, in fact, the number of contacts that can realistically occur, and hence need to be enforced in the simulation, is much reduced because the motion of the reflector is symmetric, and because each hinge —apart from the the hub hinge— is fitted with a mechanical stop that prevents it from going beyond the fully-deployed angle.

Therefore, two types of unilateral constraints will be considered. Type 1: rotations φ_2-φ_5 will be subject to unilateral constraints simulating stops when these angles reach their fully-deployed values; for hinge 1 the rotation constraint is set to prevent further closing after this hinge has reached its fully-folded angle. Type 2: distance constraints will be enforced between selected points at the corners of panels of wing 2 and selected panels of wing 1. A full list of the constraints that are considered is given in Table 1.

Type 1 constraints represent restrictions on hinge rotations through simple lower or upper bounds

$$\begin{aligned} g_1 &= -\varphi_5 - 90^\circ \geq 0 \quad , \qquad (15) \\ g_2 &= -\varphi_4 \geq 0 \quad , \qquad (16) \\ g_3 &= -\varphi_3 \geq 0 \quad , \qquad (17) \\ g_4 &= -\varphi_2 + 90^\circ \geq 0 \quad , \qquad (18) \\ g_5 &= \varphi_1 + 180^\circ \geq 0 \quad . \qquad (19) \end{aligned}$$

The gradient and the Hessian matrix of these constraint functions, which are needed when

evaluating the first-order equilibrium equations, see Section 3 of the companion paper, are

$$\nabla g_1 = \begin{bmatrix} 0 & 0 & 0 & 0 & -1 \end{bmatrix}^T \quad , \quad \nabla^2 g_1 = 0 \quad , \tag{20}$$

$$\nabla g_2 = \begin{bmatrix} 0 & 0 & 0 & -1 & 0 \end{bmatrix}^T \quad , \quad \nabla^2 g_2 = 0 \quad , \tag{21}$$

$$\nabla g_3 = \begin{bmatrix} 0 & 0 & -1 & 0 & 0 \end{bmatrix}^T \quad , \quad \nabla^2 g_3 = 0 \quad , \tag{22}$$

$$\nabla g_4 = \begin{bmatrix} 0 & -1 & 0 & 0 & 0 \end{bmatrix}^T \quad , \quad \nabla^2 g_4 = 0 \quad , \tag{23}$$

$$\nabla g_5 = \begin{bmatrix} 1 & 0 & 0 & 0 & 0 \end{bmatrix}^T \quad , \quad \nabla^2 g_5 = 0 \quad . \tag{24}$$

Type 2 constraints prevent specified points C_i, at the corners of certain panels of wing 2, see Figure 3, from penetrating specified panels of wing 1. The sub-problem depicted in Figure 6 must be solved. Here, Qi $(i = 1, \ldots, 4)$ are the four corners of a flat panel, C is a point that might come into contact with the panel, and F is the perpendicular projection of C onto the panel. Denoting the global coordinates of these points respectively by q_i, c and f, and defining

$$r_1 = q_2 - q_1 \quad , \tag{25}$$

$$r_2 = q_3 - q_2 \tag{26}$$

a vector normal to panel $Q1Q2Q3Q4$ (note that the corners of the panel need to be numbered in an anti-clockwise sense) is obtained by taking the cross-product of r_1 and r_2

$$n = \widetilde{r_1} r_2 \quad , \tag{27}$$

where $\widetilde{r_1}$ is the skew symmetric matrix associated with the vector r_1 through

$$\tilde{a} = \begin{bmatrix} 0 & -a_3 & a_2 \\ a_3 & 0 & -a_1 \\ -a_2 & a_1 & 0 \end{bmatrix} \quad \text{for} \quad a = \begin{bmatrix} a_1 \\ a_2 \\ a_3 \end{bmatrix} \quad . \tag{28}$$

In order to ensure that point C does not penetrate panel $Q1Q2Q3Q4$ we require that the distance between point C and the panel should be non-negative, which is equivalent to requiring

$$g = (c - q_1)^T n \geq 0 \quad . \tag{29}$$

Differentiating this constraint function with respect to the generalized coordinate φ_i we obtain

$$g_{,\varphi_i} = (c_{,\varphi_i} - q_{1,\varphi_i})^T n + (c - q_1)^T n_{,\varphi_i} \tag{30}$$

where

$$n_{,\varphi_i} = \widetilde{r_1} r_{2,\varphi_i} - \widetilde{r_2} r_{1,\varphi_i} \quad , \tag{31}$$

$$r_{1,\varphi_i} = q_{2,\varphi_i} - q_{1,\varphi_i} \quad , \tag{32}$$

$$r_{2,\varphi_i} = q_{3,\varphi_i} - q_{2,\varphi_i} \tag{33}$$

The second-order derivatives are

$$\begin{aligned} g_{,\varphi_i\varphi_j} = & (c_{,\varphi_i\varphi_j} - q_{1,\varphi_i\varphi_j})^T n + (c_{,\varphi_i} - q_{1,\varphi_i})^T n_{,\varphi_j} \\ & + (c_{,\varphi_j} - q_{1,\varphi_j})^T n_{,\varphi_i} + (c - q_1)^T n_{,\varphi_i\varphi_j} \end{aligned} \tag{34}$$

where

$$n_{,\varphi_i\varphi_j} = \widetilde{r_1} r_{2,\varphi_i\varphi_j} - \widetilde{r_2} r_{1,\varphi_i\varphi_j} + \widetilde{r_1}_{,\varphi_j} r_{2,\varphi_i} + \widetilde{r_1}_{,\varphi_i} r_{2,\varphi_j} \quad , \tag{35}$$

$$r_{1,\varphi_i\varphi_j} = q_{2,\varphi_i\varphi_j} - q_{1,\varphi_i\varphi_j} \quad , \tag{36}$$

$$r_{2,\varphi_i\varphi_j} = q_{3,\varphi_i\varphi_j} - q_{2,\varphi_i\varphi_j} \quad . \tag{37}$$

The constraint expressed by Equation 29 is enforced only if point F lies inside the convex polygon $Q1Q2Q3Q4$. Defining

$$r_3 = q_4 - q_3 \quad , \tag{38}$$

$$r_4 = q_1 - q_4 \tag{39}$$

this is equivalent to requiring that the cross-products of $(f - q_i)$ and r_i, for $i = 1, \ldots, 4$, should all point in the same direction, i.e. the following conditions should hold

$$-(f - q_2)^T \widetilde{r_2} \widetilde{r_1} (f - q_1) \geq 0 \quad , \tag{40}$$

$$-(f - q_3)^T \widetilde{r_3} \widetilde{r_1} (f - q_1) \geq 0 \quad , \tag{41}$$

$$-(f - q_4)^T \widetilde{r_4} \widetilde{r_1} (f - q_1) \geq 0 \quad , \tag{42}$$

where

$$f = c - g \frac{n}{n^T n} \tag{43}$$

Here, we have assumed $\widetilde{r_1}(f - q_1) \neq 0$, but any other non-zero cross-product could be used as a reference.

Of the eight Type 2 constraints, it turns out that two of them, 10 and 11, never become strongly active. The points involved in the formulation of the remaining constraints are defined

in Table 2, where the points Xi, $i = 1, \ldots, 8$, and Ci, $i = 1, 2, 4, 5$, are defined in Figure 3. In analogy with Section 3, the position vectors of these points in the hub-centred coordinate system are found to be

$$
\begin{aligned}
{}^4x_1 &= A_1B_1 \begin{bmatrix} 1 & 0 & 0 & 0 \end{bmatrix}^T , && (44)\\
{}^4x_2 &= A_1B_1 \begin{bmatrix} 1 & 0 & 0 & -L/\sqrt{3} \end{bmatrix}^T , && (45)\\
{}^4x_3 &= A_1B_1B_2 \begin{bmatrix} 1 & 0 & 0 & L/\sqrt{3} \end{bmatrix}^T , && (46)\\
{}^4x_4 &= A_1B_1B_2 \begin{bmatrix} 1 & 0 & 0 & -2L/\sqrt{3} \end{bmatrix}^T , && (47)\\
{}^4x_5 &= A_1B_1B_2B_3 \begin{bmatrix} 1 & 0 & 0 & 2L/\sqrt{3} \end{bmatrix}^T , && (48)\\
{}^4x_6 &= A_1B_1B_2B_3 \begin{bmatrix} 1 & 0 & 0 & -\sqrt{3}L \end{bmatrix}^T , && (49)\\
{}^4x_7 &= A_1B_1B_2B_3B_4 \begin{bmatrix} 1 & 0 & 0 & \sqrt{3}L \end{bmatrix}^T , && (50)\\
{}^4x_8 &= A_1B_1B_2B_3B_4 \begin{bmatrix} 1 & 0 & 0 & -4L/\sqrt{3} \end{bmatrix}^T , && (51)
\end{aligned}
$$

and

$$
\begin{aligned}
{}^4c_1 &= A_2B_1 \begin{bmatrix} 1 & 0 & 0 & -L/\sqrt{3} \end{bmatrix}^T , && (52)\\
{}^4c_2 &= A_2B_1B_2 \begin{bmatrix} 1 & 0 & 0 & -2L/\sqrt{3} \end{bmatrix}^T , && (53)\\
{}^4c_4 &= A_2B_1B_2 \begin{bmatrix} 1 & 0 & 0 & L/\sqrt{3} \end{bmatrix}^T , && (54)\\
{}^4c_5 &= A_2 \begin{bmatrix} 1 & 0 & 0 & L/2 \end{bmatrix}^T , && (55)
\end{aligned}
$$

Partial derivatives with respect to the coordinates φ_i are then obtained as in Section 3, from which all required gradients and Hessians are found. The derivatives of the potential energy, Equations 13-14, and of the constraint functions, defined above, define all quantities required to compute the first-order equilibrium equations of the reflector, i.e. Equations 43 and 44 in the companion paper.

5 Simulation results

The equilibrium path of the reflector was traced by integrating the first-order equilibrium equations of the system with the function `ode45` in Matlab (Mathworks 1997), initially using the

control parameter p as the integration variable. The starting point for the integration was the fully folded configuration; here the active constraints are not linearly independent and hence, the constraint reactions are not uniquely defined. However, it can be shown that the left- and right-hand side path derivatives of the generalized coordinates are unique.

The equilibrium path in the six-dimensional space $(\varphi_1, \varphi_2, \ldots, p)$ can be visualised through its projections onto the $\varphi_i - p$ planes, shown in Figure 7. It is interesting that, whereas the projection onto $\varphi_1 - p$ resembles the classical shape of a system with snap through, the other projections are much more complex.

The system exhibits a *corner limit point* $L1$ and a *common limit point* $L2$, see Figure 7.

At point $L1$ constraints 2 and 7 are strongly active and constraint 13 is weakly active. In order to determine the path derivatives at point $L1$ the following linear complementarity problem (LCP) was solved (see Equations 48-49 of the companion paper)

$$\dot{g}_0 = G\dot{\lambda}_0 + \dot{p}\hat{g} = -0.0015\dot{\lambda}_0 - 0.0269\dot{p} \quad , \dot{g}_0 \geq 0, \quad \dot{\lambda}_0 \geq 0, \quad \dot{g}_0^T \dot{\lambda}_0 = 0 \quad , \tag{56}$$

where g_0 and λ_0 are the values of the constraint function and the Lagrange multiplier, respectively, for the weakly active constraint 13. The $(\dot{})$ denotes a right-hand side derivative with respect to the path parameter.

Since the factors of $\dot{\lambda}_0$ and $\dot{p}$ are negative, the LCP has two solutions for $\dot{p} < 0$ and no solution for $\dot{p} > 0$, corresponding to the case of a corner limit point where the path reaches a maximum, see Section 4.2 of the companion paper.

The stability of the equilibrium path changes at $L1$, as discussed in general for corner limit points in Section 5 of the companion paper. Between $L1$ and $L2$ the path is unstable, and hence this part of the path has been plotted by a thin line. Other parts the path, which are stable have been plotted in bold.

It should be noted that at $p = -148.5°$, i.e. close to $L2$, the integrator stopped because the reduced Hessian of the Lagrangian is nearly singular. Hence, following Section 7 of the companion paper, the value of c_1 —defined in Equation 69 of the companion paper— was computed

$$c_1 = w_1^T T_+^T \nabla_\varphi U' = 8.8001 \quad , \tag{57}$$

Because $c_1 \neq 0$ and there are no weakly active constraints, the simulation is getting close to a common limit point ($\dot{p} = 0$). To choose a suitable coordinate to switch to, we compute the eigenvector w_1 associated with the zero eigenvalue of the reduced Hessian, and the matrix T_+

whose columns span the nullspace of the transposed constraint matrix E_+. For a more detailed explanation, see Sections 2.1 and 7 of the companion paper. The product of w_1 by T_+ is

$$w_1^T T_+^T = -10^{-1}[6.1871 \quad 2.0013 \quad 6.0255 \quad -2.9629 \quad 3.5534] \quad . \tag{58}$$

and, because the largest value in this row vector is the first element, we choose φ_1 as the integration variable near $L2$.

The equilibrium path that we have just obtained can be used to predict the deployment behaviour that should be expected. Starting from the fully-folded configuration, $p = -180°$, the reflector deploys following the (stable) equilibrium path. Initially, only φ_4 and φ_5 vary as the outermost panels are the only ones that can move, see also Figure 8. When $p \approx -135°$ φ_4 reaches its upper limit and shortly afterwards φ_3 starts to increase. As p is further increased, φ_3 and φ_5 are the only coordinates that vary, until the corner limit point $L1$ is reached. At $L1$, there is a dynamic snap to point $M1$, as indicated by the arrows in Figure 7. Notice that one coordinate, φ_1, changes the most; φ_2 and φ_3 also change, by smaller amounts, whereas φ_4 does not change and φ_5 changes very little. From $M1$, the antenna starts following another stable part of the equilibrium path. Plots of the configurations of the antenna before and after the snap can be seen in Figure 8.

Further increasing p causes the antenna to advance on the equilibrium path until the final, fully-deployed configuration is reached. Note that φ_1 and φ_2 are the coordinates that vary the most during this final phase.

Next, consider the retraction behaviour of the reflector, obtained by examining the behaviour of the model while following the equilibrium path with p decreasing. The system follows the equilibrium path well past $M1$, until it reaches the common limit point $L2$. Notice that the range of configurations between $M1$ and $L2$, compare Figure 8 and Figure 9, had not been seen during the deployment phase. At $L2$ the shape of the antenna is "conical," with most of the hinge lines directed towards a point above the hub. During the snap to $M2$ the overall diameter of the antenna suddenly decreases, as it changes into a more "cylindrical" shape. After the snap the reflector returns to its initial configuration following the stable equilibrium path along which it had originally deployed.

6 Comparison between simulation and experiments

Figure 10 shows a sequence of photographs taken during the deployment of a 1.5 m diameter model of the reflector. The hub is held fixed while six identical DC motors rotate the revolute joints between the connecting rod and the last panel of each wing.

The weight of the wings is offloaded through a simple gravity compensation system, consisting of six steel cables that are attached to points near the inner edge of panel 5. These cables go over pulleys suspended from an overhead support that expands in a way that mirrors the reflector, and are finally attached to counterweights. Although the centre of mass of each wing does not coincide with the suspension point in all configurations of the reflector, its position does not vary much because more than half of the weight of a wing is concentrated in the motor and its attachment. Therefore, in analysing this system it is reasonable to neglect the potential energy due to gravity, as assumed in Section 2.

Friction at points of contact between panels of the model has been virtually eliminated by attaching to the panels small ball supports that allow every possible contact point to slide smoothly over any panel with which it might come into contact.

The deployment sequence that is observed in the experiments, Figure 10, is in good qualitative agreement with that predicted by the simulation. A sudden movement of the reflector, with each wing rotating as a rigid body to a more horizontal position, does indeed occur at a stage of deployment where the simulation had predicted a dynamic snap.

For a more detailed comparison of simulation and experiment, in Figure 11 we have plotted the measured variation of the hinge angles, $\varphi_1, \ldots, \varphi_5$, vs the variation of p for a particular wing of the reflector. This was measured by Gardiner (1996), using a position and orientation measurement system that consists of a fixed transmitter and a number of small sensors attached to the panels of the reflector (Ascension 1995). The transmitter emits a pulsed DC magnetic field that is simultaneously measured by all of the sensors. Each sensor is thus able to compute its position and orientation from the magnitude and intensity of the magnetic field, which it then sends on to a personal computer.

After carrying out a series of calibration experiments, aimed at minimising the interference of the DC motors that drive the reflector and of the lab environment on the measurements taken by the system, Gardiner measured the variation during deployment (but not retraction) of all hinge angles. Her measurements confirmed that all hinges driven by motors move almost symmetrically, but there is some asymmetry in the motion of the other hinges. Figure 11 shows

a set of experimental results based on Gardiner's measurements, but scaled so that the range of each hinge angle matches the flat dish that is analysed in this paper. The detailed deployment sequence measured by Gardiner varies somewhat from wing to wing, but the plots shown are typical.

Comparing these experimental measurements to the predictions obtained in Section 5, which are also plotted in Figure 11, we find that all important features of the actual behaviour of the reflector appear to have been captured by the simulation. In particular, large variations in φ_1, φ_2 and φ_3 occur at values of p that are a little lower than the values at which the simulation predicts a snap from the corner limit point L1. Note that p does not remain constant while these shape changes occur, but slowly increases because the DC motors are continuously driven with finite velocity. For $p > -95°$, the shapes of the measured φ_1-p and φ_2-p curves do not match closely the approximately linear predictions; it is likely that this is an effect of having modelled the curved panels as flat in our analysis.

Apart from this discrepancy, the order in which all hinges reach their stops is correctly predicted, and it is remarkable that the variation of φ_3, φ_4 and φ_5 with p matches our predictions quite well.

During retraction of the reflector, Figure 12, the characteristic conical configuration predicted for $p \approx -148.5°$, Figure 9 is clearly seen. Several attempts were made to verify the prediction of a reverse snap into a configuration close to fully-folded when $p \to -180°$, but it could not be confirmed. Instead of snapping to $M2$ upon reaching configuration $L2$, the model showed very significant elastic deformation of the corner of panel 5 to which the connecting rod is attached. Further study of the simulation results showed that the driving torques become very large as $p \to -180°$, and so it is not surprising to observe a large elastic deformation of the model.

Because panel 5 was modelled as rigid, like all others, in our simulation it is to be expected that our predictions will not be accurate when $p \to -180°$. We believe that the unaccounted elastic deformation changes the shape of the equilibrium path, so that $L2$ moves further down in our plots. Hence, a value $p < -180°$ would be required in order to observe the reverse snap. In practice, the design of our model does not allow us to reach this range of angles and, even if the driving hinges were modified, it is possible that the panels would fracture under the large torques applied to them.

7 Discussion

We have presented a simulation of the deployment/retraction of a simplified version of a solid surface deployable reflector recently developed at Cambridge University. The simulation takes proper account of the contacts that can develop between panels of adjacent wings of the reflector, by implementing the theory for tracing the equilibrium path of a multibody system with unilateral constraints, proposed in the companion paper (Schulz and Pellegrino 1999).

A physical model of the reflector deploys automatically, as expected, but does not return to the starting configuration when the direction of turning of its motors is reversed. This puzzling behaviour had been impossible to explain until now.

We had previously shown (Schulz and Pellegrino, 1998) that multibody systems consisting of rigid links and elastic springs can exhibit "multi-path" behaviour similar to that observed in the model reflector when at least two different limit points exist on the equilibrium path. In the companion paper we have shown that systems with unilateral constraints exhibit, in addition to the well-known type of "common limit points," a new kind of limit point that we have called "corner limit point."

To understand what goes on during a deployment/retraction cycle of the model reflector, it is important to realise that its equilibrium path contains both a corner limit point and a common limit point, so that an appropriate simulation method can be adopted. Then, it is a relatively simple matter to compute the complete equilibrium path for the reflector, subject to certain simplifying assumptions on the geometry of the reflector and the way in which elasticity is distributed within it. Thus, one can show that during deployment the reflector will reach the corner limit point and snap to a more stable configuration. In practice, the reflector cannot snap with infinite velocity, but instead moves at a visibly faster rate near the limit point.

During retraction the equilibrium path is followed in the opposite sense, and the reflector remains on the second stable part of the path well beyond the point where it joined the path during deployment. Therefore, during retraction one observes a range of configurations that had not been seen during deployment. If the reflector is allowed to continue along this second part of the equilibrium path, eventually it will reach a common limit point, from which it will jump back to first part of the path. However, reaching this point involves very large bending and twisting moments on the panels of the model, which cause a significant amount of elastic deformation, that had not been accounted for in the computation of the equlibrium path. For this reason, we were unable to verify this aspect of our prediction.

Instead, during retraction we have to intervene manually, applying relatively small forces that cause the reflector to jump from the second stable part of the path to the first. This is possible, of course, because of the existence of two relatively close equilibrium configurations that are both stable, for the same value of the control parameter p, for $-148.5° < p < -92.1°$.

Acknowledgements

We thank Dr S.D. Guest for making available to us design and experimental data on the solid surface reflector model, and also for helpful comments. We also thank Mr P.J. Knott for assistance with the experimental work. Support from the European Commission, in the form of a TMR Marie Curie Research Training Grant for M. Schulz, and from the Royal Academy of Engineering, in the form of a Foresight Award for S. Pellegrino, is gratefully acknowledged.

References

Ascension Technology Corporation (1995). The Flock of Birds position and orientation measuring system. Installation and operation guide. Burlington, Vermont.

Denavit, J. and Hartenberg, R.S. (1955). A kinematic Notation for Lower-Pair Mechanisms Based on Matrices, *Journal of Applied Mechanics*, 215-221.

Denavit, J., Hartenberg, R.S., Razi, R. and Uicker, J.J. Jr., (1965). Velocity, Acceleration, and Static-Force Analyses of Spatial Linkages, *Journal of Applied Mechanics*, 903-910.

Gardiner, C. J. (1996). Structural instabilities in a deployable antenna. 4th-year Project Report. Department of Engineering, University of Cambridge.

Guest, S. D. and Pellegrino, S. (1996). A new concept for solid surface deployable antennas. *Acta Astronautica*, **38**, 103-113.

MathWorks (1997). Matlab User's Guide, version 5. South Natick, MA.

Schulz, M. and Pellegrino, S. (1998). "Multi-path" motion of deployable structures. In: Proceedings of Fourth World Congress on Computational Mechanics, 29 June-2 July, Buenos Aires (Edited by S. R. Idelsohn, E. Onate and E. N. Dvorkin), CIMNE, Barcelona.

Schulz, M. and Pellegrino, S. (1999). Equilibrium paths of multibody systems with unilateral constraints. Part 1: Theory. Submitted for publication.

Constraint no.	Description	Element(s) affected
1	fully opened	hinge 5
2	fully opened	hinge 4
3	fully opened	hinge 3
4	fully opened	hinge 2
5	fully closed	hinge 1
6	possible contact	C1 - panel 2
7	possible contact	C1 - panel 3
8	possible contact	C2 - panel 3
9	possible contact	C2 - panel 4
10	possible contact	C3 - panel 4
11	possible contact	C3 - panel 5
12	possible contact	C4 - panel 3
13	possible contact	C5 - panel 2

Table 1: Unilateral constraints.

Constraint no.	C	Q1	Q2	Q3	Q4
6	C1	X1	X2	X4	X3
7	C1	X3	X4	X6	X5
8	C2	X3	X4	X6	X5
9	C2	X5	X6	X8	X7
12	C4	X3	X4	X6	X5
13	C5	X1	X2	X4	X3

Table 2: Contacts between panels of adjacent wings.

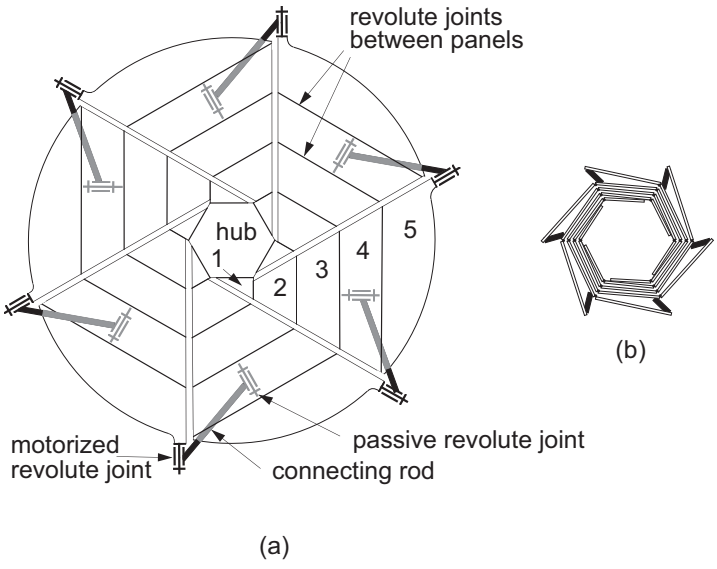

Figure 1: Rigid-panel deployable antenna (a) Fully deployed; (b) Fully folded, the panels are shown flat for clarity

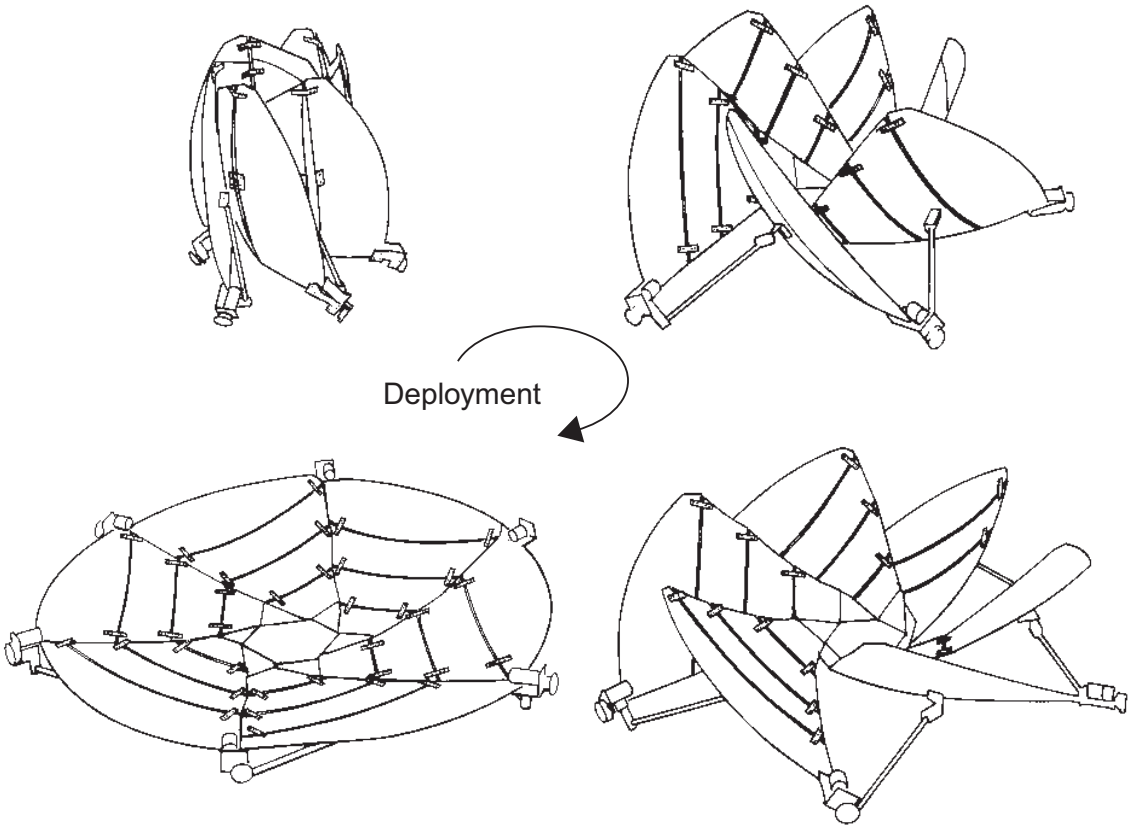

Figure 2: Antenna deployment

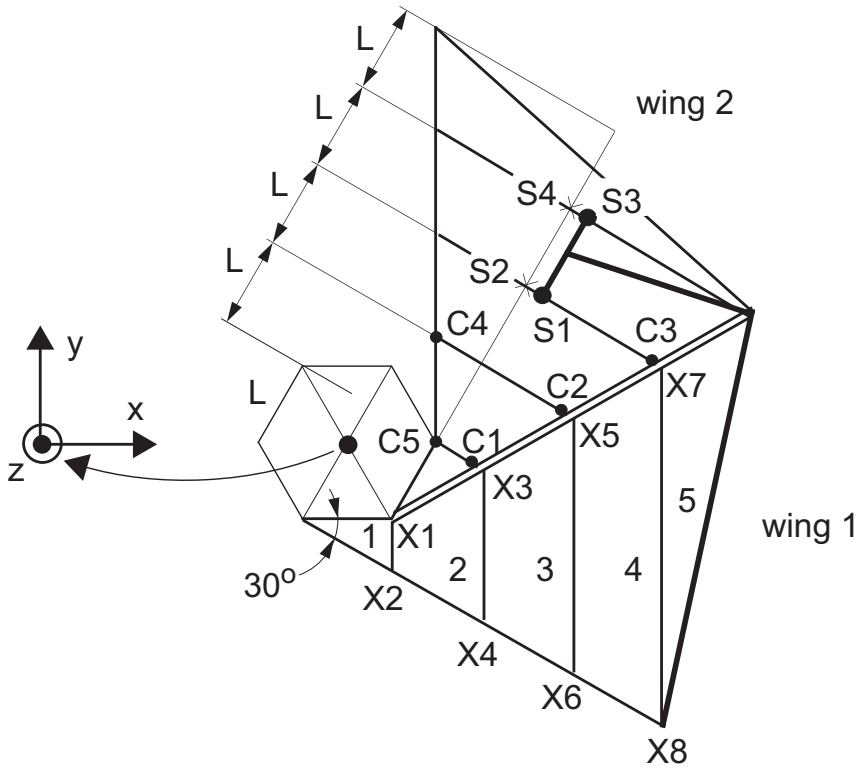

Figure 3: Simulation model

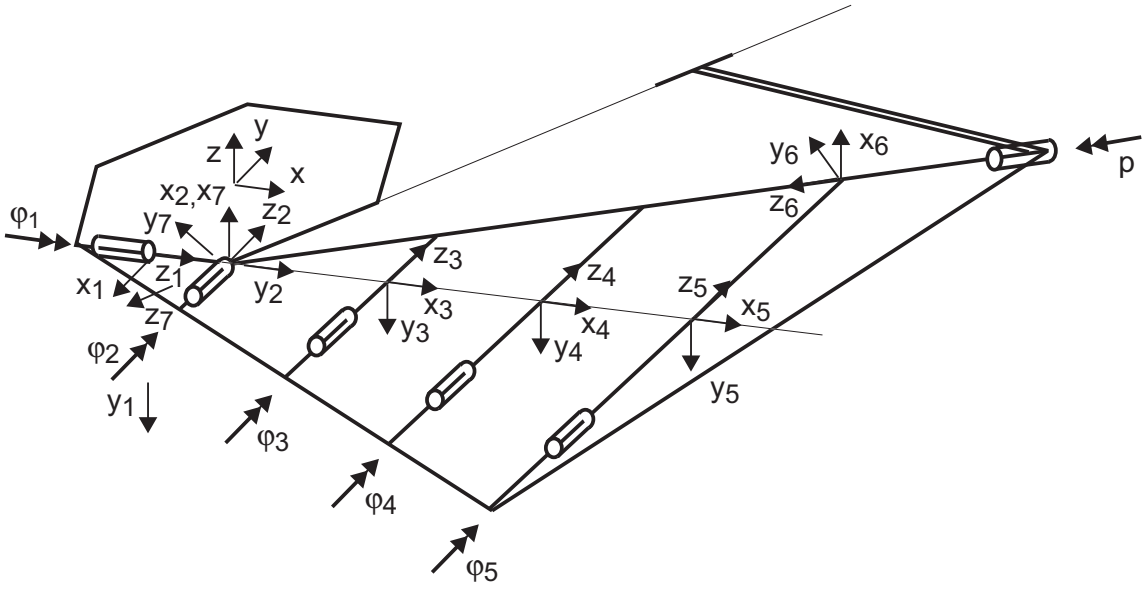

Figure 4: Definition of sets of axes (deployed configuration).

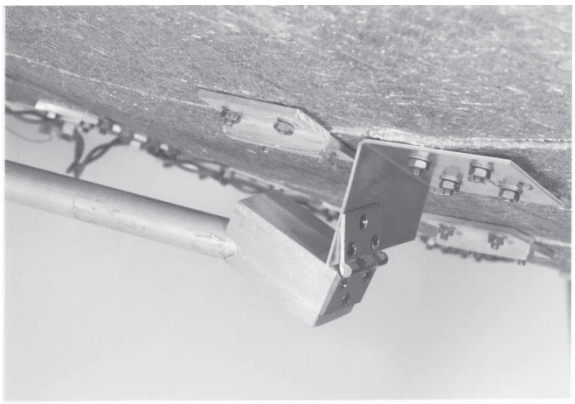

Figure 5: Al-alloy bracket between connecting rod and panel 4.

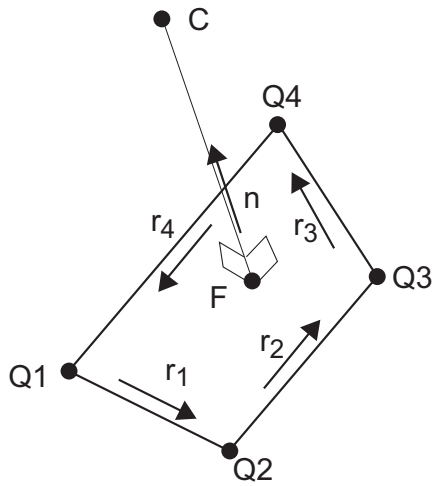

Figure 6: Unilateral contact between point C on wing 2 and a panel of wing 1

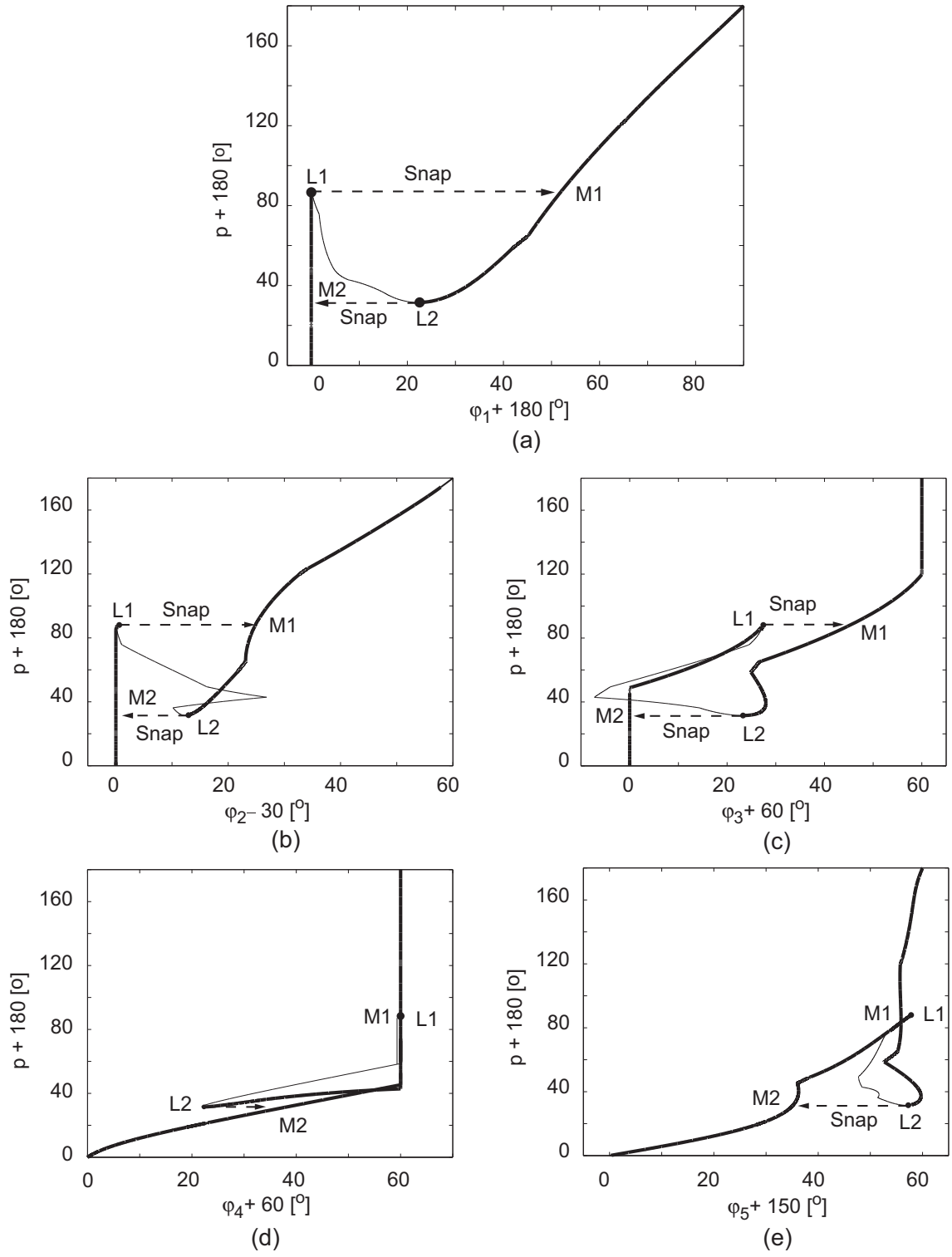

Figure 7: Equilibrium path.

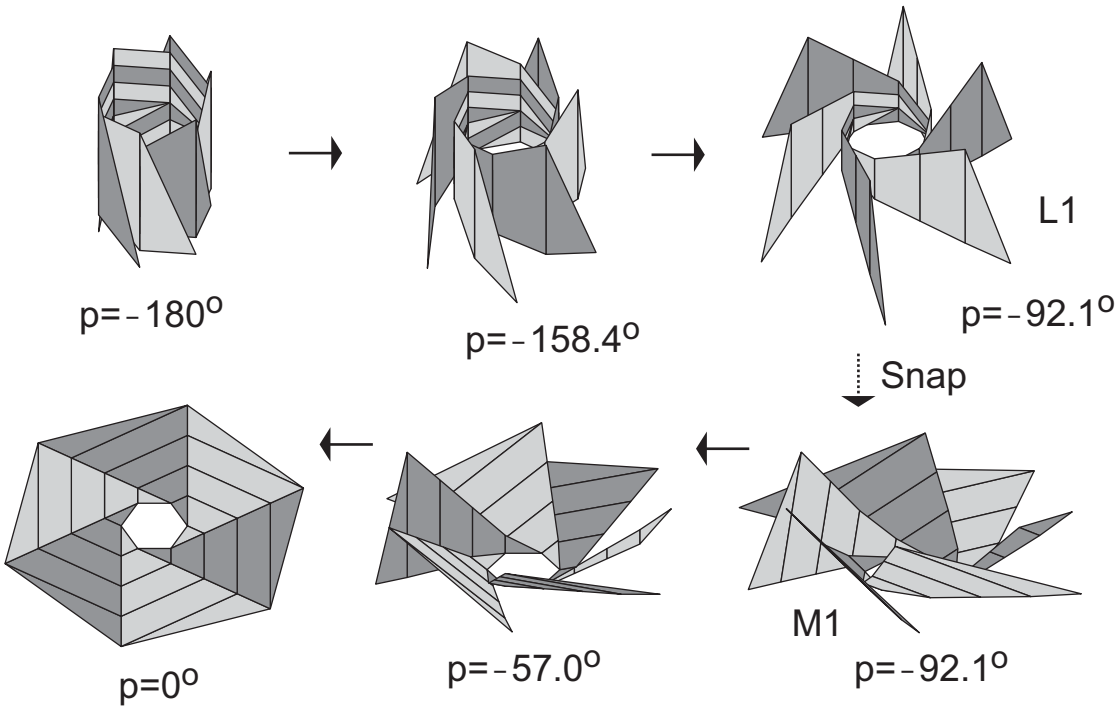

Figure 8: Simulation of antenna deployment (connecting rods not shown).

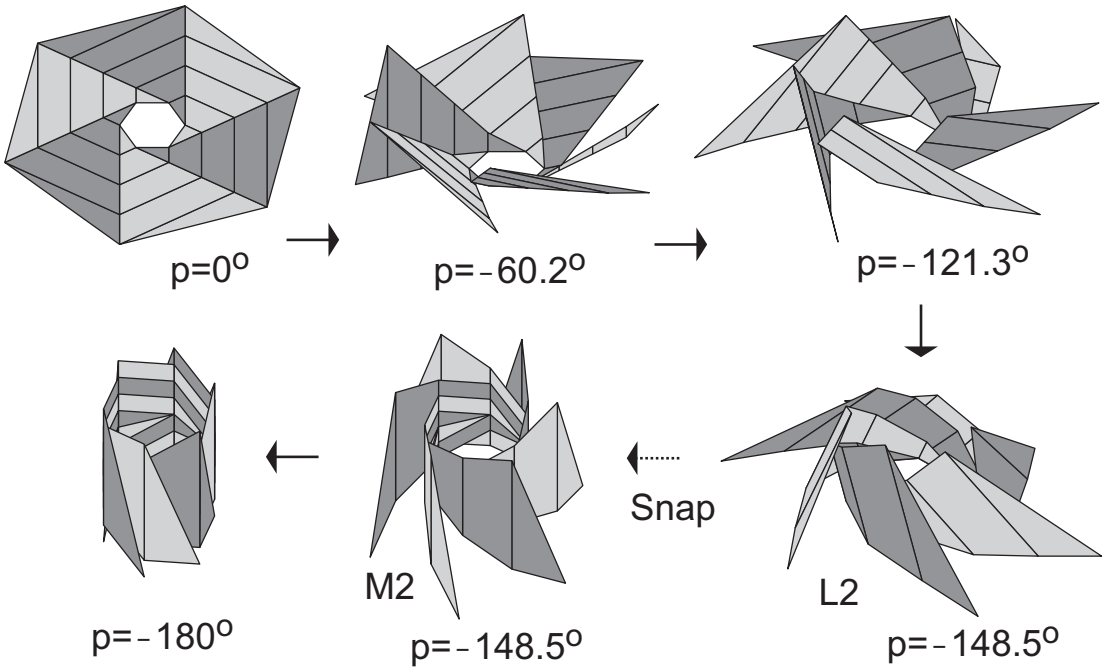

Figure 9: Simulation of antenna retraction (connecting rods not shown).

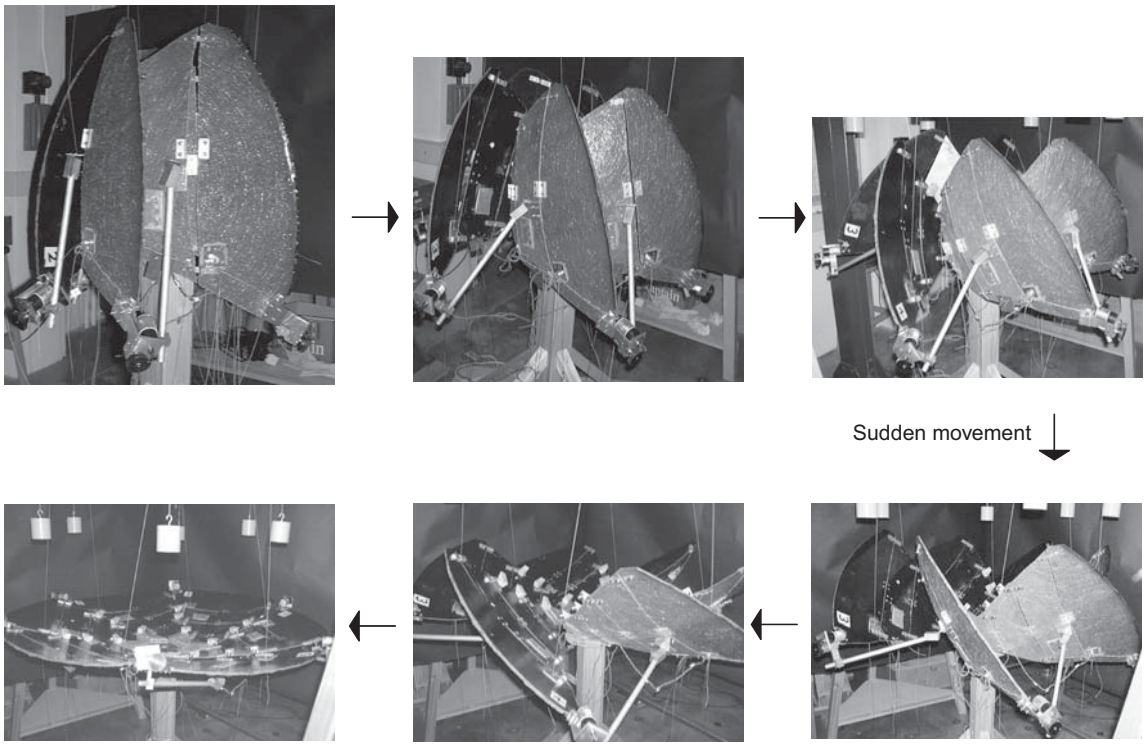

Figure 10: Deployment of physical model.

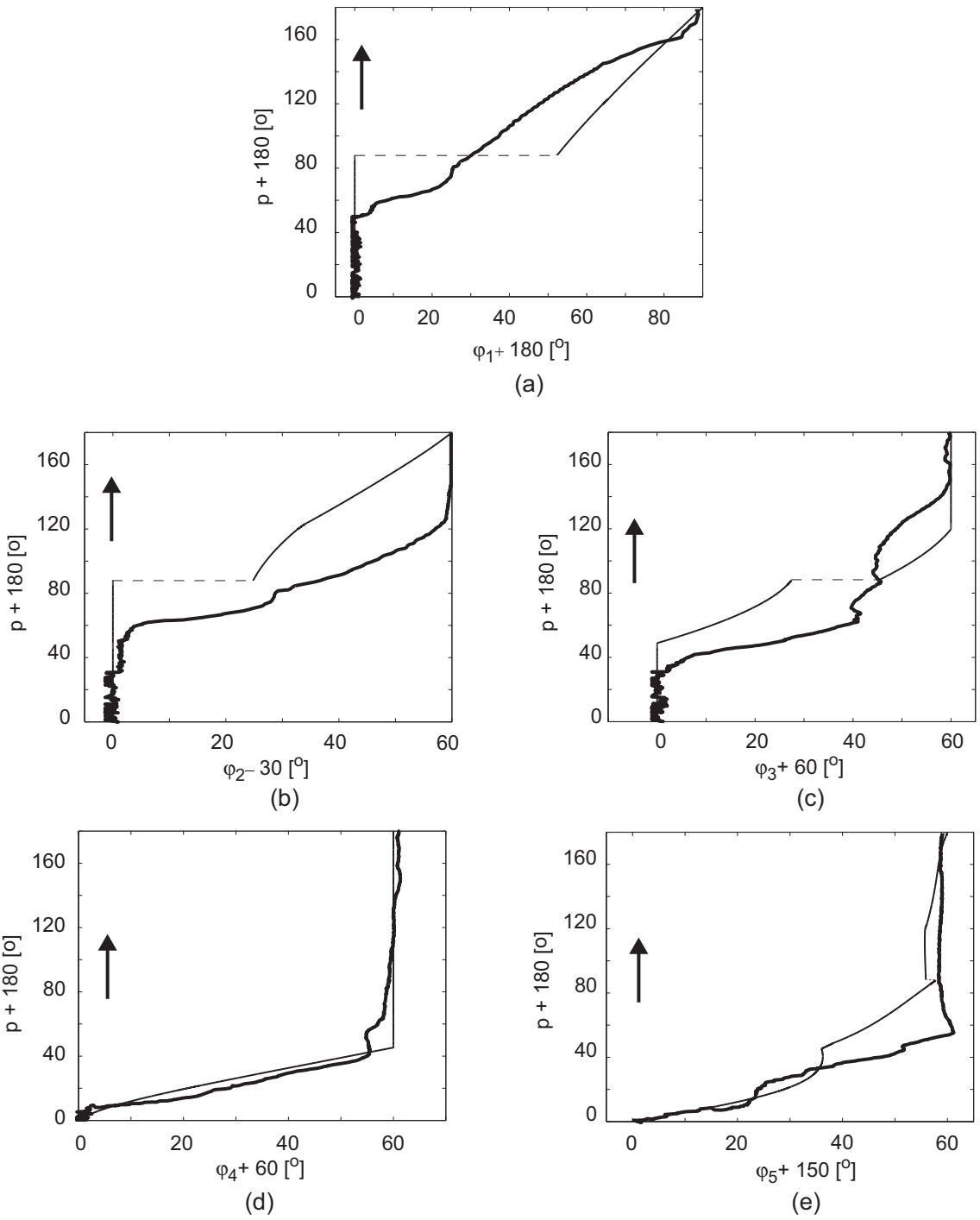

Figure 11: Variation of hinge angles during deployment, comparison of simulation (thin lines) and experiment (thick lines).

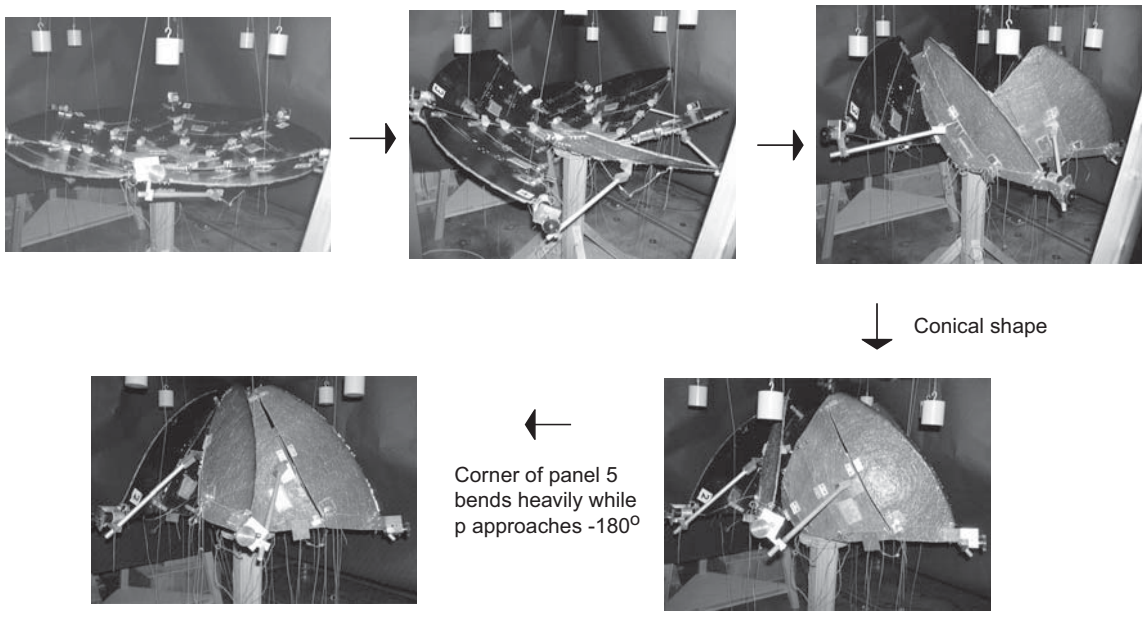

Figure 12: Retraction of physical model.

List of Figures